TISSUE ENGINEERING: Part C
Volume 19, Number 3, 2013

DOI: 10.1089/ten.tec.2012.0326

Investigation of Neovascularization in Three-Dimensional Porous Scaffolds *In Vivo* by a Combination of Multiscale Photoacoustic Microscopy and Optical Coherence Tomography

Xin Cai, MS,[*] Yu Zhang, MS,[*,†] Li Li, PhD,[‡] Sung-Wook Choi, PhD,[§] Matthew R. MacEwan, BSE, Junjie Yao, MS, Chulhong Kim, PhD,[**] Younan Xia, PhD,[†] and Lihong V. Wang, PhD

It is a grand challenge to visualize and assess *in vivo* neovascularization in a three-dimensional (3D) scaffold noninvasively, together with high spatial resolution and deep penetration depth. Here we used multiscale photoacoustic microscopy (PAM), including acoustic-resolution PAM (AR-PAM) and optical-resolution PAM (OR-PAM), to chronically monitor neovascularization in an inverse opal scaffold implanted in a mouse model up to 6 weeks by taking advantage of the optical absorption contrast intrinsic to hemoglobin molecules in red blood cells. By combining with optical coherence tomography (OCT) based on optical scattering contrast, we also demonstrated the capability to simultaneously image and analyze the vasculature and the scaffold in the same mouse. The hybrid system containing OR-PAM and OCT offered a fine lateral resolution of $\sim$5 μm and a penetration depth of $\sim$1 mm into the scaffold/tissue construct. AR-PAM further extended the penetration depth up to $\sim$3 mm at a lateral resolution of $\sim$45 μm. By quantifying the 3D PAM data, we further examined the effect of pore size (200 vs. 80 μm) of a scaffold on neovascularization. The data collected from PAM were consistent with those obtained from traditional invasive, labor-intensive histologic analyses.

Introduction

Tissue engineering integrates elements of scaffold design, cellular control, and molecular signaling to enhance the healing or replacement of an injured tissue.[1–3] In addition to its function as a physical support, a three-dimensional (3D) porous scaffold also provides a controllable microenvironment for angiogenesis, a critical step in the process of wound healing or tissue repairing.[4–7] In spite of many years of research, it remains a grand challenge to noninvasively monitor and assess the development of neovasculature *in vivo* with high spatial resolution, deep penetration, and high contrast.[7] In assessing neovascularization in implanted scaffolds, the most widely used imaging modalities include X-ray microcomputed tomography (micro-CT) and laser scanning optical microscopies (LSMs, e.g., confocal and multiphoton microscopy).[8,9] While micro-CT can penetrate a tissue/scaffold construct up to several centimeters thick, it suffers from poor contrast for soft tissues and fluid-perfused scaffolds unless exogenous contrast agents are administered. LSMs have limited tissue penetration (up to several hundred micrometers deep only), especially in the presence of strong light scattering by blood,[10] and they usually require the use of a fluorescent chromophore as the probe as well. Thus, new imaging techniques with high resolution, deep penetration, and high label-free contrast are needed to allow for noninvasive monitoring of the process of neovascularization within 3D scaffolds.

Photoacoustic microscopy (PAM) is a newly developed modality that acquires images in a noninvasive manner. It relies on photoacoustic signals generated from an object that absorbs either pulsed or intensity-modulated laser irradiation. The nonionizing irradiation used for PAM imaging is safer to tissues than the ionizing X-rays used in micro-CT.[11] Additionally, hemoglobin, the primary carrier of oxygen in blood, exhibits a strong intrinsic optical absorption contrast

Department of Biomedical Engineering, Washington University in St. Louis, St. Louis, Missouri.
*These two authors contributed equally to this work.
[†]*Current affiliation:* The Wallace H. Coulter Department of Biomedical Engineering, Georgia Institute of Technology and Emory University, Atlanta, Georgia.
[‡]*Current affiliation:* Wellman Center for Photomedicine, Massachusetts General Hospital and Harvard Medical School, Boston, Massachusetts.
[§]*Current affiliation:* Department of Biotechnology, The Catholic University of Korea, Bucheon, Korea.
**Current affiliation:* Department of Biomedical Engineering, University at Buffalo, The State University of New York, Buffalo, New York.

for label-free PAM with high sensitivity.[12] This unique feature allows one to map the vascular network and avoid possible alternations to the hemodynamics caused by exogenous angiographic agents. We have recently applied PAM to tissue engineering in an effort to resolve cell distribution in a porous polymeric scaffold *in vitro*.[13,14] In this work, we further extended the capability of PAM to demonstrate its capability in noninvasive imaging and monitoring of the neovascularization process in a porous scaffold *in vivo* for the same mouse up to 6 weeks postimplantation. When combined with optical coherence tomography (OCT), which is based on optical scattering contrast from the scaffold, we could easily resolve and compare the neovasculature developed inside the pores of the scaffolds as a function of time. In addition, we also evaluated the effect of pore size on neovascularization by quantifying the 3D PAM data.

Materials and Methods

Preparation of inverse opal scaffolds

Poly(D, L-lactide-*co*-glycolide) (PLGA) inverse opal scaffolds were fabricated by templating against gelatin lattices, which were obtained after thermal fusion of cubic closed-packed gelatin microspheres with uniform sizes. We produced the microspheres using a simple microfluidic device according to our previously published protocols[15,16] (see Supplementary Data for more details; Supplementary Data are available online at www.liebertpub.com/tec).

Animals

PLGA inverse opal scaffolds were cut into a square shape with dimensions of approximately 3 (width) × 3 (length) × 1.5 mm (height) and subcutaneously implanted in the ears of nude mice (see Supplementary Data for details on surgery and histology).

PAM and OCT

Mice with implanted scaffolds were noninvasively monitored for up to 6 weeks using an acoustic-resolution PAM (AR-PAM) (Supplementary Fig. S1A) and a hybrid system combining optical-resolution PAM (OR-PAM) and OCT (Supplementary Fig. S1B). Volumetric data were collected and processed using custom MATLAB (MathWorks, Natick) programs (see Supplementary Data for more details).

Statistics

All the results were presented as mean ± standard error for each experimental group. Three mice were monitored for chronic PAM/OCT imaging, and the other three mice were sacrificed for histology analyses at each time point. Quantification was obtained by analyzing at least 10 images randomly chosen within the region of interest from each animal (in the case of histology), or by volumetric signal processing in each animal (in the case of PAM imaging).

Results

Inverse opal scaffolds

Figure 1A shows a scanning electron microscope (SEM) image of a cubic close-packed lattice of gelatin microspheres after it had gone through thermal treatment to induce necking between adjacent spheres. This lattice then served as a sacrificial template to produce a PLGA inverse opal scaffold via an infiltration freeze-drying process. Figure 1B shows a typical SEM image of such an inverse opal scaffold. When viewed from the top, it is obvious that the inverse opal scaffold had an ordered, interconnected pore structure, together with a uniform and well-controlled pore size of about 200 μm. An enlarged view in the inset clearly shows the uniform windows that connect one pore with three pores underneath it. Figure 1C shows an SEM image of the same scaffold at a tilted angle and a lower magnification

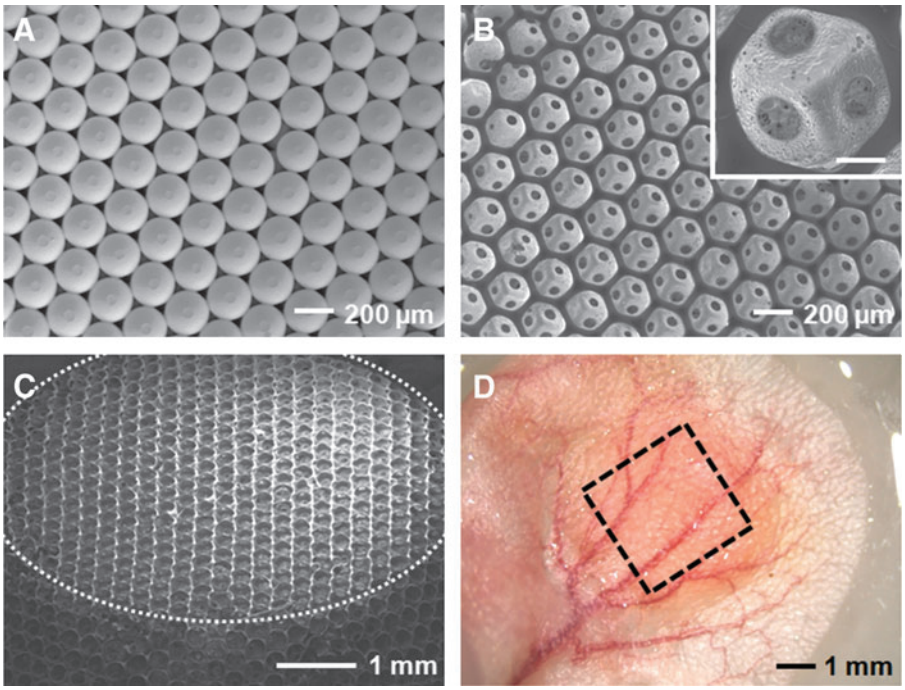

FIG. 1. Characterization of inverse opal scaffolds. SEM images showing **(A)** a cubic close-packed lattice of gelatin microspheres after thermal annealing, **(B)** a PLGA inverse opal scaffold with a pore size of 200 μm, with the inset showing an enlarged view (scale bar: 50 μm), and **(C)** the PLGA scaffold at a tilted angle to show its 3D structure and overall uniformity. The top surface of the scaffold is indicated by the dotted line. **(D)** A typical optical micrograph showing an inverse opal scaffold (marked by a square) implanted subcutaneously in the ear of a nude mouse. SEM, scanning electron microscope; PLGA, poly(D, L-lactide-*co*-glycolide); 3D, three-dimensional. Color images available online at www.liebertpub.com/tec

where the top surface is indicated by the dotted line, revealing its three-dimensionality and structural uniformity.

OR-PAM and OCT of neovascularization in inverse opal scaffolds

Supplementary Figure S1A shows a schematic of the dual-modality system that combines OR-PAM and spectral-domain OCT.[17] The OR-PAM subsystem used a diode-pumped Nd:YVO4 laser, and the photoacoustic signals were detected using a focused ultrasonic transducer. The OR-PAM subsystem had a lateral resolution of 5 μm by using optical focusing and an axial resolution of 14 μm. The OCT subsystem measures the light backscattered from the object (e.g., the polymeric scaffold), and was characterized by a lateral resolution of 5 μm and an axial resolution of 5.9 μm. Both OR-PAM and OCT had a penetration depth of ~1 mm in high-scattering soft tissues, such as skin.

PLGA inverse opal scaffolds with a pore size of ~200 μm in diameter of $\sim 3 \times 3 \times 1.5\,mm^3$ in dimensions were implanted subcutaneously in the ears of nude mice (one scaffold per ear per mouse, Fig. 1D), and monitored using the dual-modality OR-PAM/OCT system at an excitation wavelength of 532 nm up to 6 weeks postimplantation. In this study, the PLGA polymer itself could not generate sufficiently strong PA signals to provide adequate contrast, and thus only vasculature was imaged by the PAM due to the strong optical absorption of hemoglobin. As shown by the maximum amplitude projection (MAP) images in Figure 2A–C and the movie in Supplementary Movie S1, the density of blood vessels increased with time over the 6-week period. Microvasculature down to the capillary level was well resolved due to the high lateral resolution of OR-PAM. OCT signals were also collected simultaneously with PAM scanning, which were used to resolve the structure of the scaffold/tissue construct. The OCT signals from the top layer of the ear skin (~150 μm in thickness) were removed from the 3D data.[18] As shown by the MAP images in Figure 2D–F and Supplementary Movie S2, while the overall structure of the scaffold was largely retained by week 6, some regions had slightly degraded over the period, leading to a local increase in the size of a few pores (examples are indicated by arrowheads).

Figure 3A–C and Supplementary Movie S3 show coregistered 3D depictions of the vasculature (in red) and the scaffold/tissue construct (in green). The growth of a neovasculature into the scaffold started before week 4, as revealed by co-localization of the blood vessels and the pores on the surface of the scaffold (Fig. 3B, C, marked by arrowheads). Figure 3D–F show the corresponding coregistered B-scan (z-direction) images at the positions indicated by the dotted lines in Figure 3A–C, respectively. Several layers of the pores close to the surface of the scaffold could be clearly resolved in the OCT images. Blood vessels were seen to gradually develop over time from the surrounding tissue into the interior of the scaffold. Some vessels could reach a depth of more than 1 mm at week 6 (Fig. 3F). In these images, OCT signals from the skin were removed to clearly show the surface of the scaffold.[18]

AR-PAM of neovascularization in inverse opal scaffolds

A schematic of the AR-PAM is shown in Supplementary Figure S1B.[12] This system used a dye laser pumped by an Nd:YLF laser, and the photoacoustic wave was detected by a

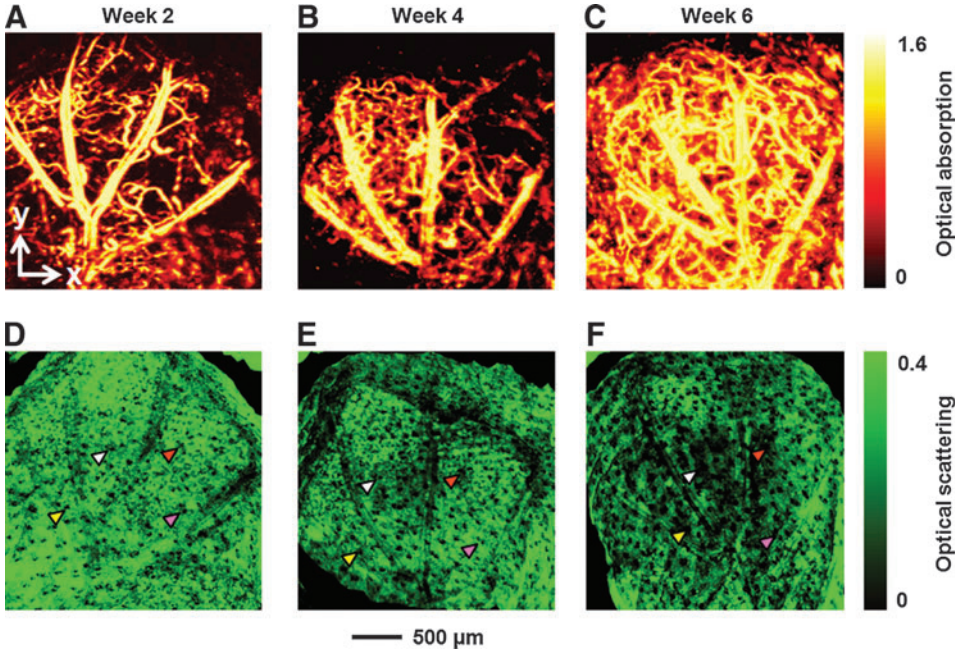

FIG. 2. Chronic OR-PAM and OCT images showing the vasculature and scaffold/tissue construct for an inverse opal scaffold with a pore size of 200 μm. **(A–C)** PAM MAP images showing the development of blood vessels at 2, 4, and 6 weeks postimplantation, respectively. **(D–F)** The corresponding OCT MAP images showing the scaffold/tissue construct. MAP stands for maximum amplitude projection. The signals from the skin layer were removed from all the OCT images to show the surface of the scaffold more clearly. Arrowheads indicate examples of local increase in pore size over time due to degradation of the scaffold. PAM, photoacoustic microscopy; OR-PAM, optical-resolution PAM; OCT, optical coherence tomography. Color images available online at www.liebertpub.com/tec

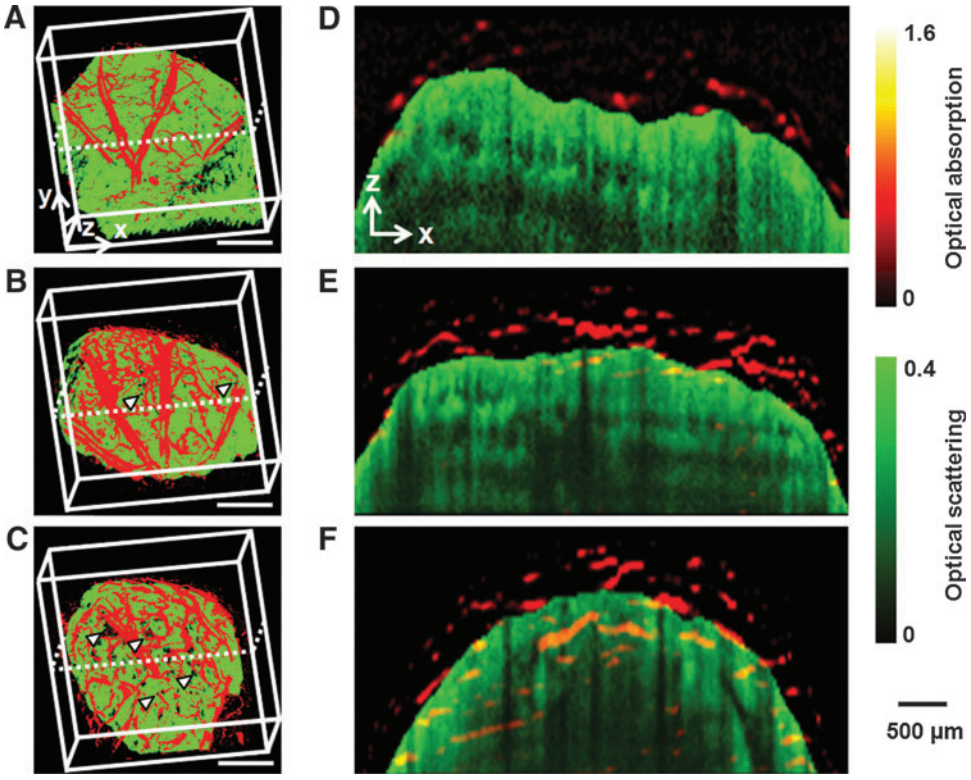

FIG. 3. Chronic OR-PAM and OCT coregistered images showing the development of neovasculature in the same scaffold as in Figure 2. **(A–C)** Coregistered 3D depictions of the vasculature (red) and scaffold/tissue construct (green) at 2, 4, and 6 weeks postimplantation, respectively. The arrowheads indicate the growth of neovasculature into the pores of the scaffold (scale bars: 500 μm). **(D–F)** Coregistered B-scan images at the planes indicated by dotted lines in **(A–C)**, respectively, showing the gradual inward growth of blood vessels into the inner pores of the scaffold. The signals from the skin layer were removed from all the OCT images to clearly show the boundaries between the blood vessels outside and inside the scaffold. Color images available online at www.liebertpub.com/tec

focused ultrasonic transducer. The optical focal spot size was 2 mm in diameter, much larger than that of the OR-PAM (5 μm). Therefore, the lateral resolution was predominantly determined by the narrower ultrasonic focus. The AR-PAM could achieve a lateral resolution of 45 μm, an axial resolution of 15 μm, and a penetration depth of ~3 mm in soft tissues. This system was chosen for the following studies, because it provides deeper penetration than OR-PAM while maintaining an adequate image resolution.

The same group of mice was also monitored by AR-PAM at an excitation wavelength of 570 nm at 1, 2, 4, and 6 weeks postimplantation (Fig. 4). At 1 week postimplantation, the area of the scaffold (indicated by the white dotted square) could be clearly resolved due to the absence of blood vessels (Fig. 4A). The scaffold could be better resolved in Figure 4E after removal of the signals from the skin (~150 μm in thickness) using an algorithm similar to what was used for the OCT images.[18] As shown by Figure 4B–D and Supplementary Movie S4, the neovasculature developed gradually over time, consistent with the observations by OR-PAM depicted in Figure 2A–C. These blood vessels not only grew on top of the implanted scaffold but also penetrated into the scaffold, as shown by the images in Figure 4F–H, where the signals from the skin layer have been removed from the 3D PAM data. In addition, B-scan images (Fig. 4I–L) at the indicated positions (green dotted lines in Fig. 4A–D) show increase both in the signal intensity and the number of blood vessels in the central regions, confirming the inward growth of a neovasculature into the inner pores of the scaffold.

To further demonstrate the capability of our imaging modality, we implanted inverse opal scaffolds with a pore size of ~80 μm (Supplementary Fig. S2) into the ears of a new group of mice. The mice were then noninvasively monitored by AR-PAM at 1, 2, 4, and 6 weeks postimplantation (Fig. 5 and Supplementary Movie S5). As shown in the images where the signals from skin layer had been removed from the 3D PAM data, the neovasculature essentially did not efficiently regenerate into the scaffold region until week 4 (Fig. 5E–G). Even by week 6 (Fig. 5H), there were significantly fewer blood vessels inside the scaffold, and they took up much smaller areas than those inside the scaffold with a pore size of 200 μm (Fig. 4H). The corresponding B-scan images also show much fewer blood vessels inside the scaffold (Fig. 5I–L).

Histology and correlation with quantitative PAM

A group of mice with implanted PLGA inverse opal scaffolds (200 and 80 μm in pore size) were sacrificed and subjected to histology analyses at the same time points as the PAM imaging. Figure 6A–C shows typical hematoxylin and eosin (H&E)-stained sections from the center (500–1000-μm below the surface) of the scaffolds with a pore size of 200 μm at 2, 4, and 6 weeks postimplantation, respectively. A few blood vessels (indicated by arrowheads) with small diameters could be observed starting at week 2 (Fig. 6A), and they grew both in number and area over time (Fig. 6B, C). By contrast, for scaffolds with a pore size of 80 μm, only a small number of blood vessels with small total areas could be observed even at week 6 (Fig. 6E–G). These observations were qualitatively consistent with the PAM images (Figs. 4 and 5).

Figure 7A and B show quantifications of normalized vessel area as a function of time calculated from both histology and PAM data for the scaffolds with pore sizes of 200 μm (Fig. 7A) and 80 μm (Fig. 7B), respectively. The area of blood

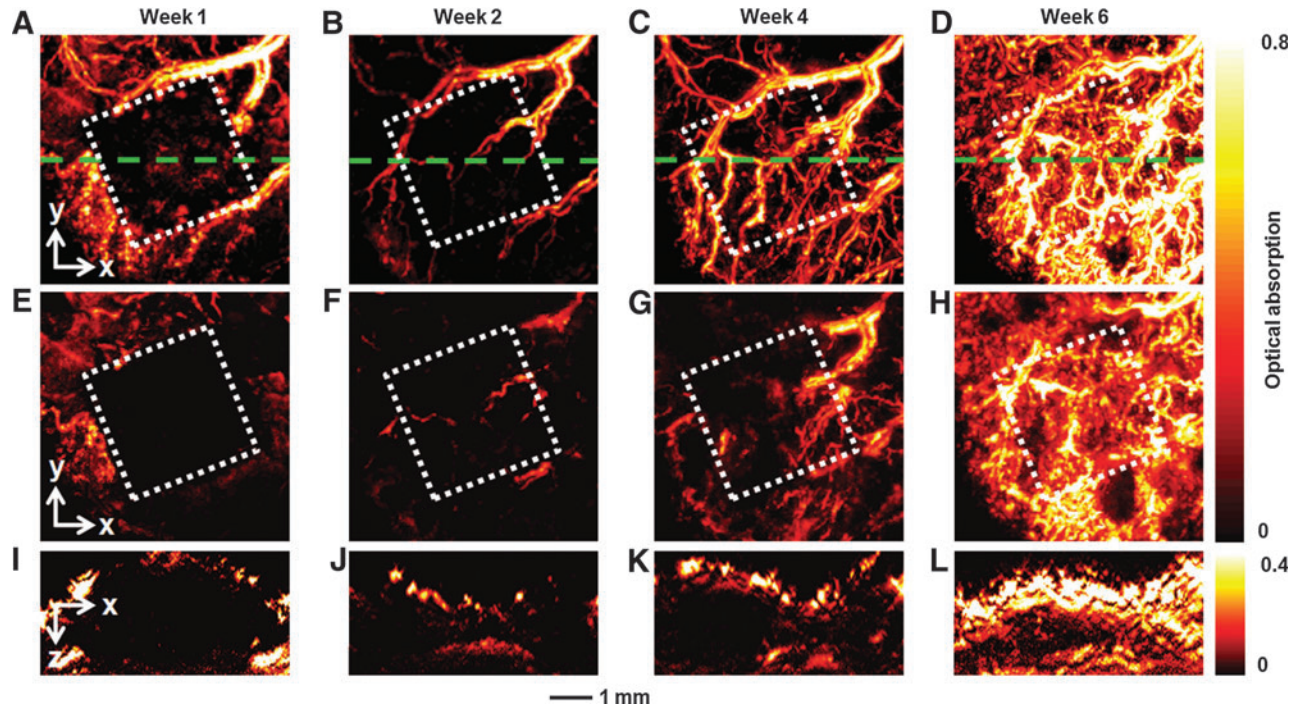

FIG. 4. Chronic AR-PAM images revealing the development of neovasculature in an inverse opal scaffold with a pore size of 200 μm. **(A–D)** MAP images without removing the signals from the skin layer on top of the scaffold at 1, 2, 4, and 6 weeks postimplantation, respectively. **(E–H)** Corresponding MAP images after removal of the signals from the skin layer on top of the scaffold. **(I–L)** The corresponding B-scan images at are planes marked by the green dashed lines in **(A–D)**, respectively. The dotted square indicates the area where the scaffold resided. AR-PAM, acoustic-resolution PAM. Color images available online at www.liebertpub.com/tec

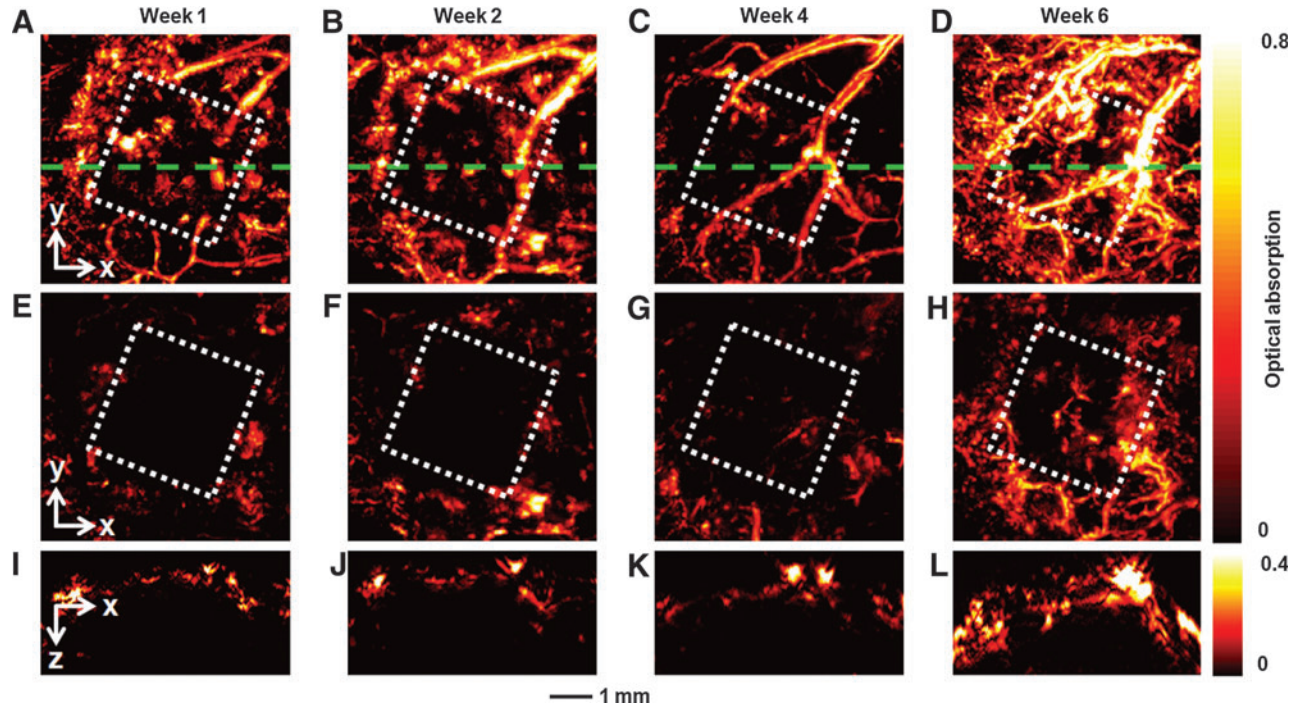

FIG. 5. Chronic AR-PAM images showing the development of neovasculature in an inverse opal scaffold with a pore size of 80 μm. **(A–D)** MAP images without removing the signals from the skin layer on top of the scaffold at 1, 2, 4, and 6 weeks postimplantation, respectively. **(E–H)** The corresponding MAP images after removing the signals from the skin layer on top of the scaffold. **(I–L)** The corresponding B-scan images at planes are marked by the green dashed lines in **(A–D)**, respectively. The dotted square indicates the region where the scaffold resided. Color images available online at www.liebertpub.com/tec

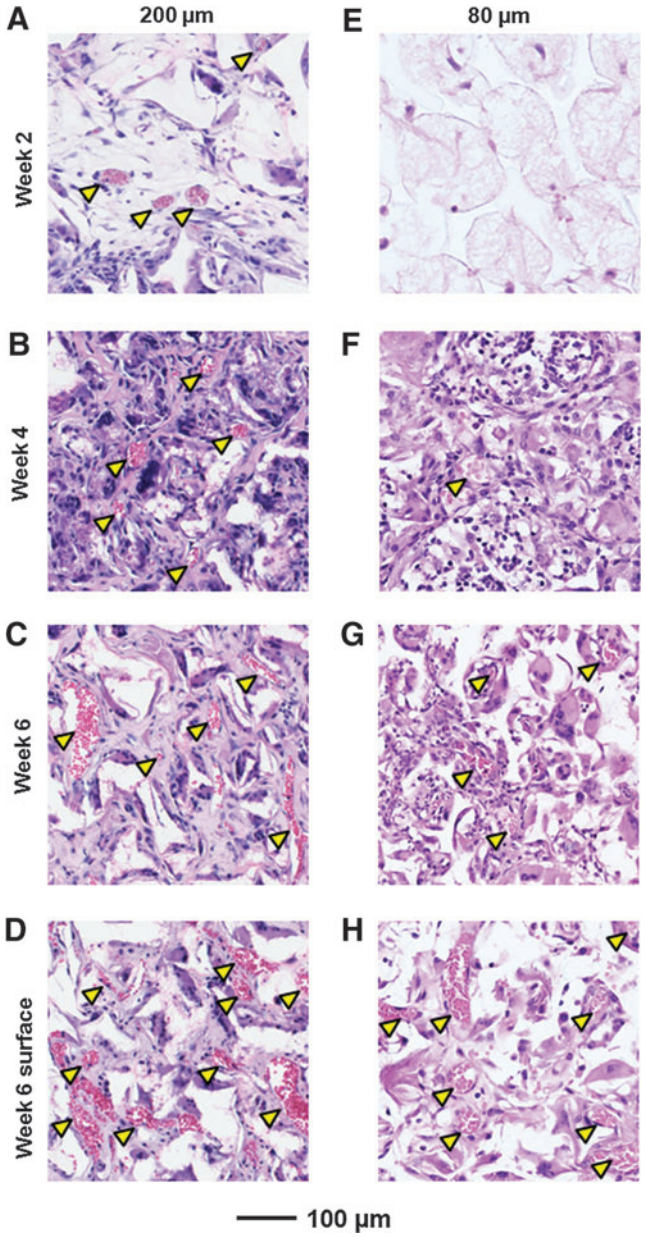

FIG. 6. Histology images showing the development of neovasculature in inverse opal scaffolds. Hematoxylin and eosin-stained sections of the explanted scaffolds with a pore size of **(A–D)** 200 µm and **(E–H)** 80 µm postimplantation at **(A, E)** 2 weeks, **(B, F)** 4 weeks, and **(C, D, G, H)** 6 weeks. Sections in **(A–C, E–G)** were obtained from the central region (500–1000 µm below surface) of the scaffolds, while sections in (**D, H**) were obtained from a plane close to the surface (0–200 µm). Arrowheads denote blood vessels. Color images available online at www.liebertpub.com/tec

vessels at each time point was normalized against that of the scaffolds with a pore size of 80 µm at week 2. The PAM results show that the normalized vessel areas for the scaffolds with a pore size of 200 µm were 2.0–3.5 times larger than those of the scaffolds with a pore size of 80 µm over a period of 6 weeks, which correlated well with the histology analyses. We further examined the development of neovasculature close to the surface (0–200 µm) of the scaffold

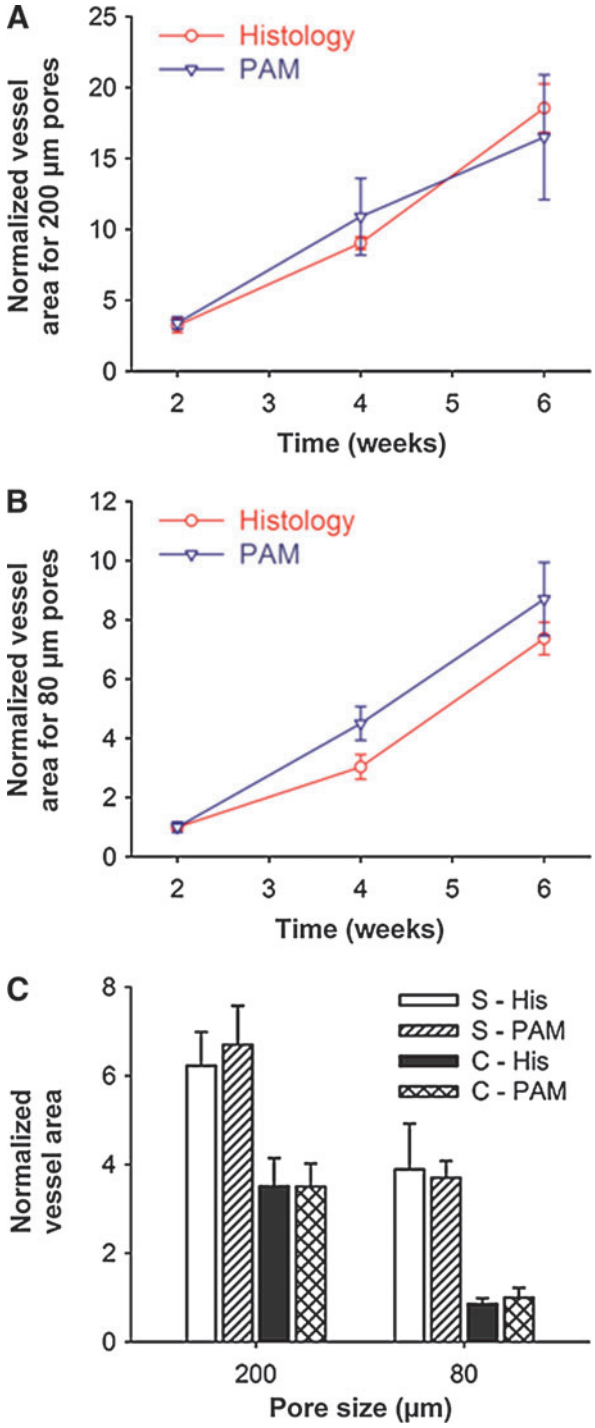

FIG. 7. Comparison of histology analyses and PAM quantification. **(A, B)** Normalized vessel area calculated from both PAM data and histology for scaffolds with a pore size of **(A)** 200 µm and **(B)** 80 µm. **(C)** A comparison of the blood vessel area in the scaffolds at planes close to the surface and in the central region of the scaffolds 6 weeks postimplantation. S, surface; C, center; His, histology. All the results were presented as mean ± standard error ($n = 3$). Color images available online at www.liebertpub.com/tec

from the PAM data (Fig. 6D, H). In both type of scaffolds, there were vessels with large areas, and the vessel areas were estimated to be ~1.9 times and ~3.7 times larger than those in the central region of the scaffolds with pore sizes of 200 and 80 μm, respectively (Fig. 7C). Similar results could also be quantified by analyzing the histology data (Fig. 7A–C).

Discussion

The PLGA inverse opal scaffolds were fabricated by templating against cubic close-packed lattices of gelatin microspheres.[13,15,19–22] As two unique features, the inverse opal scaffolds have a uniform pore size and an interconnected porous structure, which are critical to improvement of homogeneity in cell seeding throughout the entire scaffold.[20,23] As such, these scaffolds could reduce the density of defect sites that may exist in scaffolds with nonuniform pores and structures.[20] When implanted *in vivo*, these inverse opal scaffolds could also potentially induce faster and more uniform tissue/blood vessel infiltration and thus formation of a better interface between the scaffold and the surrounding tissue. Therefore, this new class of 3D porous scaffolds is well suited for tissue-engineering applications, which usually require neovascularization during the process of regeneration.[24,25]

So far, it has been difficult to temporally monitor the development of neovasculatures in 3D scaffolds with a relatively high spatial resolution and deep penetration in a noninvasive, label-free manner. Traditionally, the inward growth of blood vessels into a tissue-engineering construct is examined by either destructive methods that require the excision of the implants for histology analyses, or methods that require the use of contrast agents (e.g., micro-CT and LSMs). By contrast, PAM is a better imaging modality for chronically monitoring the growth of blood vessels *in vivo*, since it does not require any exogenous contrast agents, as its contrast mechanism is based upon the optical absorption of hemoglobin, an intrinsic component of red blood cells (RBCs).[26,27]

On the other hand, multimodality imaging has become increasingly important, as it can offer details of the hierarchical structures of a sample. In this work, we have introduced a dual-modality system combining OR-PAM and OCT, where OR-PAM could effectively monitor the development of blood vessels by taking advantage of the strong absorption of hemoglobin (Fig. 2A–C and Supplementary Movie S1), whereas OCT could give information about the structure of an implanted scaffold due to its optical scattering contrast (Fig. 2D–F and Supplementary Movie S2), both noninvasively. By coregistering the data obtained from each modality, the positions of the vessels relative to the scaffold were revealed (Fig. 3 and Supplementary Movie S3), clearly showing the gradual invasion of blood vessels into the interior of the scaffold.

Interestingly, while several layers of the pores of the scaffold could be observed under the skin layer at weeks 2 and 4 in OCT images (Fig. 3D, E), the porous structures could no longer be clearly observed at week 6 (Fig. 3F), probably due to (1) inward growth of the surrounding tissues that could blur the scattering signals from the scaffold due to their similar refractive indices[28] and (2) slight degradation of the scaffold that rendered its structure undetectable by OCT as a result of compromised material and structural properties.

For the OR-PAM subsystem, it was difficult to image deeply into the scaffold due to strong optical scattering. Therefore, we also used an AR-PAM system with a lateral resolution of 45 μm (as defined by ultrasonic focusing) for imaging studies. In this case, the invasion of vasculature from the surroundings into the implanted scaffold could be readily observed by AR-PAM (Fig. 4 and Supplementary Movie S4). Comparing images obtained using these two PAM modalities (Figs. 2–4 and Supplementary Movies S2 and S4), it can be concluded that OR-PAM was capable of achieving a better lateral resolution (5 μm) than AR-PAM, while AR-PAM allowed for a greater penetration depth of more than 3 mm, making it better suited for imaging the whole thickness of the scaffold (1.2–1.5 mm) plus that of the mouse ear (~0.5 mm). The AR-PAM system could still provide adequate resolution at such a penetration depth, because the resolution was determined by the ultrasonic parameters, and ultrasound scattering is much weaker than optical scattering in biological tissues and scaffolds. It should be emphasized that PAM is capable of imaging on multiple length scales, covering structures spanning from organelles to organs.[29] In fact, photoacoustic tomography can even image objects in biological tissues as deep as ~5.2 cm at the expense of resolution,[30,31] which may be sufficient to fit the ultimate goal of engineering tissues over large volumes.

The imaging modality could also be used to evaluate the angiogenic effect of a scaffold by resolving the growth patterns of neovascularization in different scaffolds. To this end, we did a new set of experiments with scaffolds with pores of 80 μm in size. As shown by the PAM images (Fig. 5 and Supplementary Movie S5), there was a much lower degree of vascularization in these scaffolds as compared to those with a pore size of 200 μm (Fig. 4 and Supplementary Movie S4). For scaffolds with a pore size of 80 μm, most of the neovessels could only grow into the pores close to the surface, but not deeply into the scaffold (Figs. 6E–H and 7C). The reason for this type of growth is that the small windows (15–20 μm in size) connecting adjacent pores might limit the penetration of vessels into the pores deeply inside the scaffold. By contrast, scaffolds with a pore size of 200 μm were able to allow more neovessels to infiltrate into the pores close to the surface as well as to penetrate deeply into the central region through the relatively large windows (40–50 μm), eventually leading to the formation of a network of large, interconnected blood vessels (Figs. 6A–D and 7C).

Another significant feature of PAM is its capability to quantify the signals, that is, PAM allows us not only to visualize the temporal growth of the vasculature but also to quantify the increase in the blood vessel volume inside the scaffold. By comparing the data from PAM with those from traditional histological analyses, we found that they agreed well with each other (Fig. 7A–C), indicating good accuracy of quantification by PAM. It should be pointed out that, for histology analyses, we calculated the blood vessel areas using the data from H&E-stained tissue/scaffold sections. Blood vessels were identified from the presence of RBCs surrounded with a continuous layer of (vascular) cells.[32] Although such a method cannot distinguish different types of vessels by specific markers as with immunostaining (e.g., CD31 and von Willebrand factor for endothelial cells in

capillaries[33,34] and α-smooth muscle actin for smooth muscle cells in arteries[35]), the results could be directly compared with those obtained by PAM. The reason is that PAM detects hemoglobin in RBCs in all types of blood vessels, including those newly formed (with RBCs, but without blood flow), and therefore the blood vessel areas calculated from PAM volumetric data were essentially the areas of RBCs, which should match better with those derived from histology images with simply H&E staining.

Furthermore, other important parameters of the neovasculature inside a scaffold, such as flow velocity and oxygen saturation,[36–38] can be derived by functional PAM.

Conclusions

We have demonstrated that PAM could be a powerful tool for chronically monitoring neovascularization in an inverse opal scaffold *in vivo* in a noninvasive manner. By combining with OCT, we also demonstrated the capability to simultaneously image and analyze the vasculature and scaffold. The whole scaffold/tissue (~2 mm in thickness) could be well imaged and resolved in a 3D fashion. The hybrid system containing OR-PAM and OCT offered a fine lateral resolution of ~5 μm and a penetration depth of ~1 mm into the scaffold/tissue construct. AR-PAM further extended the penetration depth up to ~3 mm at a lateral resolution of ~45 μm. By quantifying the 3D PAM data, we further examined the effect of pore size (200 vs. 80 μm) of a scaffold on neovascularization. The PAM results show that the normalized vessel areas for the scaffolds with a pore size of 200 μm were 2.0–3.5 times larger than those of the scaffolds with a pore size of 80 μm over a period of 6 weeks, which correlated well with traditional invasive, labor-intensive histology analyses. Our results suggest that PAM will become a useful imaging modality for tissue-engineering applications, especially when thick scaffold/tissue constructs are involved.

Acknowledgments

We are grateful to Lynnea Brumbaugh for close reading of the manuscript. This work was supported in part by an NIH Director's Pioneer Award (DP1 OD000798) and startup funds from the Washington University in St. Louis (to Y.X.). This work was also sponsored by the NIH grants (R01 EB000712, R01 EB008085, R01 CA140220, R01 CA157277, R01 CA159959, and U54 CA136398, to L.V.W.). Part of the research was performed at the Alafi Neuroimaging Laboratory of the Hope Center for Neurological Disorders, which was supported by the NIH Neuroscience Blueprint Center Core Grant P30 NS057105.

Disclosure Statement

L.V.W. has a financial interest in Microphotoacoustics, Inc. and Endra, Inc., which, however, did not support this work. All other authors declare no competing financial interests.

References

1. Langer, R., and Vacanti, J. Tissue engineering. Science **260,** 920, 1993.
2. Langer, R. Tissue engineering: status and challenges. E-Biomed J Regen Med **1,** 5, 2004.
3. Langer, R. Perspectives and challenges in tissue engineering and regenerative medicine. Adv Mater **21,** 3235, 2009.
4. Ma, P.X. Scaffolds for tissue fabrication. Mater Today **7,** 30, 2004.
5. Hollister, S.J. Porous scaffold design for tissue engineering. Nat Mater **4,** 518, 2005.
6. Patel, Z.S., and Mikos, A.G. Angiogenesis with biomaterial-based drug- and cell-delivery systems. J Biomater Sci Polym Ed **15,** 701, 2004.
7. Lovett, M., Lee, K., Edwards, A., and Kaplan, D.L. Vascularization strategies for tissue engineering. Tissue Eng Part B Rev **15,** 353, 2009.
8. Schmidt, C., Bezuidenhout, D., Beck, M., Van der Merve, E., Zilla, P., and Davies, N. Rapid three-dimensional quantification of VEGF-induced scaffold neovascularisation by microcomputed tomography. Biomaterials **30,** 5959, 2009.
9. Perng, C.-K., Wang, Y.-J., Tsi, C.-H., and Ma, H. *In vivo* angiogenesis effect of porous collagen scaffold with hyaluronic acid oligosaccharides. J Surg Res **168,** 9, 2011.
10. Dumas, D., Riquelme, B., Werkmeister, E., Isla, N.D., and Stoltz, J.F. Multimodality of microscopy imaging applied to cartilage tissue engineering. In: Buckwalter, J.A., Lotz, M., and Stoltz, J.-F., eds. Biomedical and Health Research. Amsterdam: IOS Press, 2007, pp. 254–266.
11. Kim, C., Favazza, C., and Wang, L.V. *In vivo* photoacoustic tomography of chemicals: high-resolution functional and molecular optical imaging at new depths. Chem Rev **110,** 2756, 2010.
12. Zhang, H.F., Maslov, K., Stoica, G., and Wang, L.V. Functional photoacoustic microscopy for high-resolution and noninvasive *in vivo* imaging. Nat Biotechnol **24,** 848, 2006.
13. Zhang, Y., Cai, X., Choi, S.-W., Kim, C., Wang, L.V., and Xia, Y. Chronic label-free volumetric photoacoustic microscopy of melanoma cells in three-dimensional porous scaffolds. Biomaterials **31,** 8651, 2010.
14. Zhang, Y., Cai, X., Wang, Y., Zhang, C., Li, L., Choi, S.-W., *et al.* Noninvasive photoacoustic microscopy of living cells in two and three dimensions through enhancement by a metabolite dye. Angew Chem Int Ed **123,** 7497, 2011.
15. Choi, S.-W., Cheong, I.W., Kim, J.-K., and Xia, Y. Preparation of uniform microspheres using a simple fluidic device and their crystallization into close-packed lattice. Small **5,** 454, 2009.
16. Choi, S.-W., Zhang, Y., and Xia, Y. Fabrication of microbeads with a controllable hollow interior and porous wall using a capillary fluidic device. Adv Funct Mater **19,** 2943, 2009.
17. Li, L., Maslov, K., Ku, G., and Wang, L.V. Three-dimensional combined photoacoustic and optical coherence microscopy for *in vivo* microcirculation studies. Opt Express **17,** 16450, 2009.
18. Zhang, H.F., Maslov, K., and Wang, L.V. Automatic algorithm for skin profile detection in photoacoustic microscopy. J Biomed Opt **14,** 024050, 2009.
19. Choi, S.-W., Zhang, Y., Thomopoulos, S., and Xia, Y. *In vitro* mineralization by preosteoblasts in poly(D, L-lactide-*co*-glycolide) inverse opal scaffolds reinforced with hydroxyapatite nanoparticles. Langmuir **26,** 12126, 2010.
20. Choi, S-W., Zhang, Y., and Xia, Y. Three-dimensional scaffolds for tissue engineering: the importance of uniformity in pore size and structure. Langmuir **26,** 19001, 2010.
21. Zhang, Y., Choi, S.-W., and Xia, Y. Modifying the pores of an inverse opal scaffold with chitosan microstructures for truly three-dimensional cell culture. Macromol Rapid Commun **33,** 296, 2012.

22. Choi, S.-W., Zhang, Y., MacEwan, M.R., and Xia, Y. Neovascularization in biodegradable inverse opal scaffolds with uniform and precisely controlled pore sizes. Adv Healthcare Mater, 2012 [Epub ahead of print]; DOI: adhm.201200106.
23. Zhang, Y., and Xia, Y. Formation of embryoid bodies with controlled sizes and maintained pluripotency in three-dimensional inverse opal scaffolds. Adv Funct Mater **22,** 121, 2012.
24. Jain, R.K., Au. P., Tam, J., Duda, D.G., and Fukumura, D. Engineering vascularized tissue. Nat Biotechnol **23,** 821, 2005.
25. Moon, J.J., and West J. L. Vascularization of engineered tissues: approaches to promote angio-genesis in biomaterials. Curr Top Med Chem **8,** 300, 2008.
26. Hu, S., Maslov, K., and Wang, L.V. Second-generation optical-resolution photoacoustic microscopy with improved sensitivity and speed. Opt Lett **36,** 1134, 2011.
27. Yao, J., Maslov, K., Zhang, Y., Xia, Y., and Wang, L.V. Label-free oxygen-metabolic photoacoustic microscopy *in vivo*. J Biomed Opt **16,** 076003, 2011.
28. Yang, Y., Dubois, A., Qin, X.-P., Li, J., Haj, A.E.I., and Wang, R.K. Investigation of optical coherence tomography as an imaging modality in tissue engineering. Phys Med Biol **51,** 1649, 2006.
29. Wang, L.V. Multiscale photoacoustic microscopy and computed tomography. Nat Photon **3,** 503, 2009.
30. Ku, G., and Wang, L.V. Deeply penetrating photoacoustic tomography in biological tissues enhanced with an optical contrast agent. Opt Lett **30,** 507, 2005.
31. Kim, C., Erpelding, T.N., Jankovic, L., Pashley, M.D., and Wang, L.V. Deeply penetrating *in vivo* photoacoustic imaging using a clinical ultrasound array system. Biomed Opt Express **1,** 278, 2010.
32. Jabbarzadeh, E., Starnes, T., Khan, Y.M., Jiang, T., Wirtel, A.J., Deng, M., *et al.* Induction of angiogenesis in tissue-engineered scaffolds designed for bone repair: a combined gene therapy-cell transplantation approach. Proc Natl Acad Sci U S A **105,** 11099, 2008.
33. Kalka, C., Masuda, H., Takahashi, T., Kalka-Moll, W.M., Silver, M., Kearney, M., *et al.* Transplantation of *ex vivo* expanded endothelial progenitor cells for therapeutic neovascularization. Proc Natl Acad Sci U S A **97,** 3422, 2000.
34. Levenberg, S., Golub, J.S., Amit, M., Itskovitz-Eldor, J., and Langer, R. Endothelial cells derived from human embryonic stem cells. Proc Natl Acad Sci U S A **99,** 4391, 2002.
35. L'Heureux, N., Dusserre, N., Konig, G., Victor, B., Keire, P., Wight, T.N., *et al.* Human tissue-engineered blood vessels for adult arterial revascularization. Nat Med **12,** 361, 2006.
36. Yao, J., and Wang, L.V. Transverse flow imaging based on photoacoustic Doppler bandwidth broadening. J Biomed Opt **15,** 021304, 2010.
37. Yao, J., Maslov, K.I., Shi, Y., Taber, L.A., and Wang, L.V. *In vivo* photoacoustic imaging of transverse blood flow by using Doppler broadening of bandwidth. Opt Lett **35,** 1419, 2010.
38. Zhang, H.F., Maslov, K., Sivaramakrishnan, M., Stoica, G., and Wang, L.V. Imaging of hemoglobin oxygen saturation variations in single vessels *in vivo* using photoacoustic microscopy. Appl Phys Lett **90,** 053901, 2007.

Address correspondence to:
Younan Xia, PhD
The Wallace H. Coulter Department of Biomedical Engineering
Georgia Institute of Technology and Emory University
Atlanta, GA 30332

E-mail: younan.xia@bme.gatech.edu

Lihong V. Wang, PhD
Department of Biomedical Engineering
Washington University in St. Louis
One Brookings Drive
St. Louis, MO 63130

E-mail: lhwang@seas.wustl.edu

Received: May 29, 2012
Accepted: July 20, 2012
Online Publication Date: September 10, 2012